A&A 601, L3 (2017)
DOI: 10.1051/0004-6361/201730851

Astronomy & Astrophysics

Letter to the Editor

First detection of the 448 GHz H_2O transition in space

M. Pereira-Santaella[1], E. González-Alfonso[2], A. Usero[3], S. García-Burillo[3], J. Martín-Pintado[4], L. Colina[4], A. Alonso-Herrero[4], S. Arribas[4], S. Cazzoli[5], F. Rico[4], D. Rigopoulou[1], and T. Storchi Bergmann[6]

[1] Department of Physics, University of Oxford, Keble Road, Oxford OX1 3RH, UK
e-mail: miguel.pereira@physics.ox.ac.uk
[2] Universidad de Alcalá, Departamento de Física y Matemáticas, Campus Universitario, 28871 Alcalá de Henares, Madrid, Spain
[3] Observatorio Astronómico Nacional (OAN-IGN)-Observatorio de Madrid, Alfonso XII, 3, 28014 Madrid, Spain
[4] Centro de Astrobiología (CSIC/INTA), Ctra de Torrejón a Ajalvir, km 4, 28850 Torrejón de Ardoz, Madrid, Spain
[5] Instituto de Astrofísica de Andalucía, CSIC, Glorieta de la Astronomía, s/n, 18008 Granada, Spain
[6] Universidade Federal do Rio Grande do Sul, Instituto de Física, CP 15051, Porto Alegre 91501-970, RS, Brazil

Received 22 March 2017 / Accepted 18 April 2017

ABSTRACT

We present the first detection of the ortho-H_2O $4_{23}-3_{30}$ transition at 448 GHz in space. We observed this transition in the local ($z = 0.010$) luminous infrared (IR) galaxy ESO 320-G030 (IRAS F11506-3851) using the Atacama Large Millimeter/submillimeter Array (ALMA). The water $4_{23}-3_{30}$ emission, which originates in the highly obscured nucleus of this galaxy, is spatially resolved over a region of ~65 pc in diameter and shows a regular rotation pattern compatible with the global molecular and ionized gas kinematics. The line profile is symmetric and well fitted by a Gaussian with an integrated flux of 37.0 ± 0.7 Jy km s^{-1}. Models predict this water transition as a potential collisionally excited maser transition. On the contrary, in this galaxy, we find that the $4_{23}-3_{30}$ emission is primarily excited by the intense far-IR radiation field present in its nucleus. According to our modeling, this transition is a probe of deeply buried galaxy nuclei thanks to the high dust optical depths ($\tau_{100\mu m} > 1$, $N_H > 10^{24}$ cm^{-2}) required to efficiently excite it.

Key words. galaxies: ISM – galaxies: nuclei – infrared: galaxies – ISM: molecules

1. Introduction

Water is a molecule of astrophysical interest because it not only plays a central role in the Oxygen chemistry of the interstellar medium (e.g., Hollenbach et al. 2009; van Dishoeck et al. 2013) but it is also one of the main coolants of shocked gas (e.g., Flower & Pineau Des Forêts 2010). In addition, thanks to its energy level structure, water couples very well to the far-infrared (far-IR) radiation field providing an effective probe of the far-IR continuum in the warm compact regions found in active galactic nuclei (AGNs) and young star-forming regions (e.g., González-Alfonso et al. 2014, hereafter GA14).

Water excitation models have long predicted the maser nature of the $4_{23}-3_{30}$ transition pumped by collisions when the kinetic temperature is $T_{kin} \sim 1000$ K and the hydrogen density $n_{H_2} \sim 10^5$ cm^{-3} (e.g., Deguchi 1977; Cooke & Elitzur 1985; Neufeld & Melnick 1991; Yates et al. 1997; Daniel & Cernicharo 2013; Gray et al. 2016). This transition can also be excited by radiative pumping through the absorption of far-IR photons (see Sect. 4 and Fig. 1). Therefore, the determination of the dominant excitation mechanism, which might vary from source to source, is required to properly interpret the $4_{23}-3_{30}$ emission as a tracer of dense hot molecular gas or as a tracer of intense IR radiation fields in compact regions.

In this letter, we present the first detection of the ortho-H_2O $4_{23}-3_{30}$ 448.001 GHz transition in space[1]. No previous detections of this transition in Galactic objects have been reported, probably because of the high atmospheric opacity due to the terrestrial water vapor. Only recently, thanks to the sensitivity of the Atacama Large Millimeter/submillimeter Array (ALMA), it became possible to observe this transition in nearby galaxies redshifted into more accessible frequencies.

We observed the H_2O $4_{23}-3_{30}$ transition in ESO 320-G030 (IRAS F11506-3851; D = 48 Mpc; 235 pc arcsec^{-1}). This object is an isolated spiral galaxy with a regular velocity field (Bellocchi et al. 2016) and an IR luminosity ($\log L_{IR}/L_\odot = 11.3$) in the lower end of the luminous IR galaxy (LIRGs) range ($11 < \log L_{IR}/L_\odot < 12$). It is a starburst object with no evidence of an AGN based on X-ray and mid-IR diagnostics (Pereira-Santaella et al. 2010, 2011), and hosts an extremely obscured nucleus ($A_V \sim 40$ mag) and a massive outflow powered by the presumed nuclear starburst detected in the ionized, neutral atomic, and molecular phases (Arribas et al. 2014; Cazzoli et al. 2014, 2016; Pereira-Santaella et al. 2016, hereafter PS16). In addition, a molecular gas inflow is suggested by the inverse P Cygni profile observed in the far-IR OH absorptions (González-Alfonso et al. 2017). It is an OH megamaser source (Norris et al. 1986), but no 22 GHz H_2O maser emission has been detected (Wiggins et al. 2016). This is consistent with the starburst activity of the nucleus of ESO 320-G030 (see Lo 2005).

2. ALMA data reduction

We obtained band 8 ALMA observations of ESO 320-G030 on 2016 November 16 using 42 antennas of the 12-m array as part of the project #2016.1.00263.S. The total on-source integration time was 10.5 min. The baselines ranged from 15 m to 920 m that

[1] Persson et al. (2007) reported a tentative detection of the water isotopologue $H_2^{18}O$ $4_{23}-3_{30}$ transition at 489.054 GHz in Orion, although it is blended with a much stronger methanol transition.

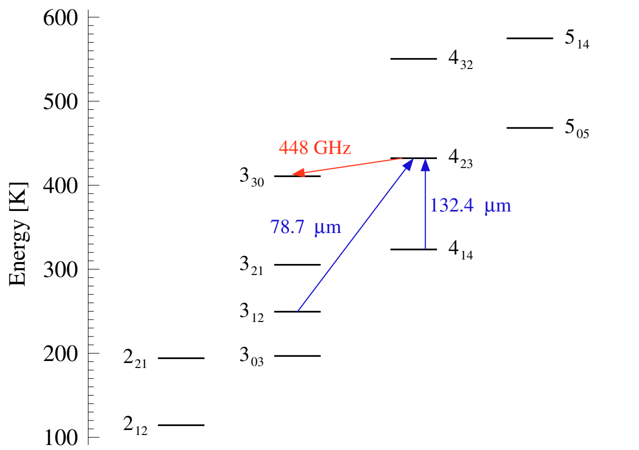

Fig. 1. Partial energy level diagram of ortho-H_2O. The $4_{23}-3_{30}$ 448 GHz transition is indicated in red. The 78.7 and 132.4 μm transitions, which populate the 4_{23} level radiatively through the absorption of far-IR photons (see Sect. 4), are marked in blue.

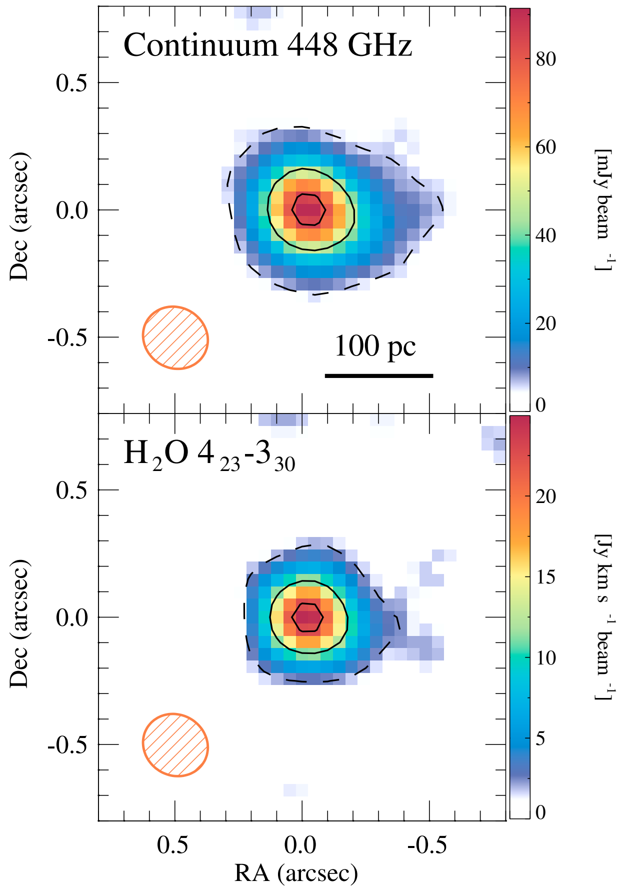

Fig. 2. Map of the 448 GHz (rest frequency) continuum (*top panel*) and zeroth moment of the H_2O $4_{23}-3_{30}$ emission (*bottom panel*) of ESO 320-G030. The dashed line contour marks the 3σ level (7 mJy beam^{-1} and 2.5 Jy km s^{-1} beam^{-1}, respectively). The solid contour lines indicate the peak × (0.5, 0.9) levels. The red hatched ellipses indicate the beam size (0.″26 × 0.″24, PA = 58°). The coordinates are relative to 11 53 11.7192 +39 07 49.105 (J2000).

correspond to a maximum recoverable scale of ~2″ based on the ALMA Cycle 4 Technical Handbook equations. A three pointing pattern was used to obtain a mosaic with uniform sensitivity over a ~8″ × 8″ field of view.

In this letter, we only use data from a spectral window centered at 443.0 GHz (1.875 GHz/1270 km s^{-1} bandwidth and 1.95 MHz/1.3 km s^{-1} channels) where the redshifted H_2O $4_{23}-3_{30}$ 448.001 GHz transition is detected. The remaining ALMA data will be analyzed in a future paper (Pereira-Santaella et al., in prep.). The data were reduced and calibrated using the ALMA reduction software CASA (v4.7.0; McMullin et al. 2007). For the flux calibration we used J1229+0203 (3C 273) assuming a flux density of 2.815 Jy at 449.6 GHz and a spectral index α = −0.78 ($f_\nu \propto \nu^\alpha$). The final data-cube has 300 × 300 pixels of 0.″05 and 31.2 MHz (20 km s^{-1}) channels. For the cleaning, we used the Briggs weighting with R = 0.5 (Briggs 1995) which provides a beam with a full-width half-maximum (FWHM) of 0.″26 × 0.″24 (~60 pc) and a position angle (PA) of 58°. The 1σ sensitivity is ~4.8 mJy beam^{-1} per channel. We corrected the data-cube for the primary beam pattern of the mosaic.

3. Data analysis

We detect continuum and line emission only in the central ~200 pc (~1″). This is consistent with the extent of the 233 GHz (1.3 mm) continuum emission in this object (see PS16). We estimated the continuum level in each pixel from the median flux density in the line-free channels of the spectral window. The resulting continuum map is shown in Fig. 2. The measured total continuum emission in the central 200 pc is 183 ± 4 mJy.

From the continuum subtracted data cube, we extracted the nuclear spectrum using a d = 0.″8 aperture (Fig. 3). A line is detected at 443 451 ± 2 MHz. This corresponds to a rest frame frequency of 448 007 ± 4 MHz (using the systemic velocity $\upsilon_{\rm radio}$ = 3049 ± 2 km s^{-1}, derived from CO(2−1); see PS16) which agrees with the frequency expected for the ortho-H_2O $4_{23}-3_{30}$ transition (448001 MHz; Pickett et al. 1998). This line identification is also supported by the detection of strong far-IR and sub-mm water transitions in the *Herschel* observations of this object (see Sect. 4). We also detect a weaker emission line (3.7±0.6 Jy km s^{-1}) which we tentatively identify as two CH_2NH transitions at ~446.8 GHz ($E_{\rm up}$ = 96 and 117 K; Pickett et al. 1998). Another two CH_2NH transitions at 447.9 and 448.1 GHz might contribute to the $4_{23}-3_{30}$ flux. However, these have $E_{\rm up} \geq$ 280 K so their contributions are likely negligible.

We fitted a Gaussian to the H_2O $4_{23}-3_{30}$ profile and the result is shown in Fig. 3. We obtained a total flux of 37.0 ± 0.7 Jy km s^{-1}, a velocity of 3045 ± 1 km s^{-1}, and a FWHM of 161 ± 2 km s^{-1}. The $4_{23}-3_{30}$ profile is symmetric and it is centered at the systemic velocity. By contrast, the nuclear CO(2−1) profile has a higher FWHM and presents a more complex asymmetric profile (see Figs. 3 and 6 of PS16).

From the 448 GHz continuum and the zeroth moment water emission maps (Fig. 2), we measured the sizes of the emitting regions by fitting a 2D Gaussian. Both the continuum and the water emission are spatially resolved in the ALMA observations with the continuum being more extended. The continuum size (FWHM) is 0.″38 × 0.″32, which, deconvolved by the beam size, corresponds to 60 pc × 50 pc at the distance of ESO 320-G030. The size of the water emission is 0.″30 ± 0.″02, which is equivalent to a deconvolved FWHM of 40 ± 3 pc. For a uniform-brightness disk, the equivalent radius is 0.8 × FWHM (Sakamoto et al. 2008), that is, R ~ 45 and 30–35 pc for the 448 GHz continuum and the H_2O line, respectively.

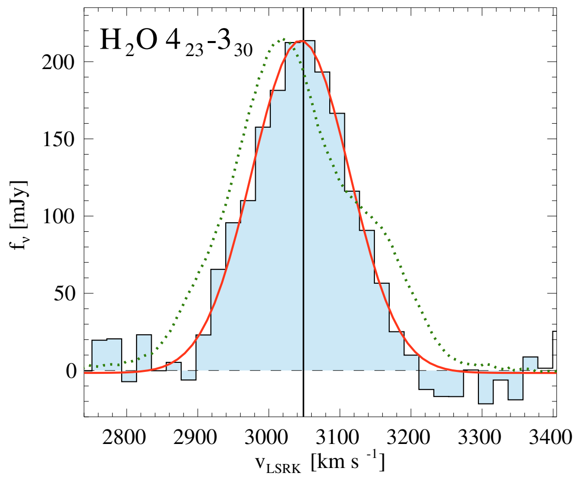

Fig. 3. Continuum subtracted profile of the H_2O 4_{23}–3_{30} 448 GHz emission in ESO 320-G030 extracted using a circular aperture with $d = 0.''8$ centered at the nucleus (see Fig. 2). The dotted green line is the normalized CO(2–1) profile extracted from the same region. The black vertical line indicates the systemic velocity derived from the CO(2–1) global kinematic model (PS16). The red solid line is the best Gaussian fit to the water profile (see Sect. 3).

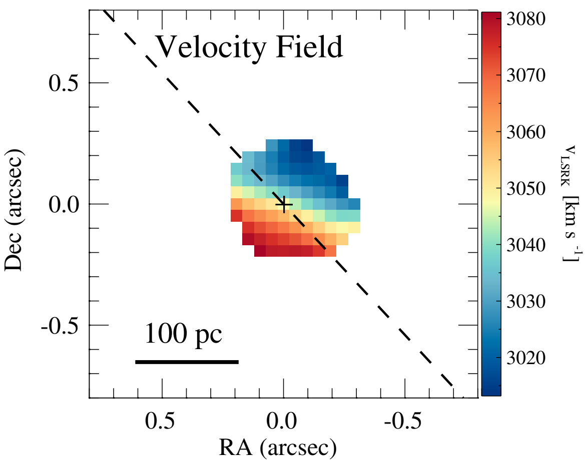

Fig. 4. Velocity field of the H_2O 4_{23}–3_{30} emission. The black cross marks the position of the water emission peak (see Fig. 2). The dashed line is the minor kinematic axis derived from the kinematic analysis of the CO(2–1) emission (see PS16).

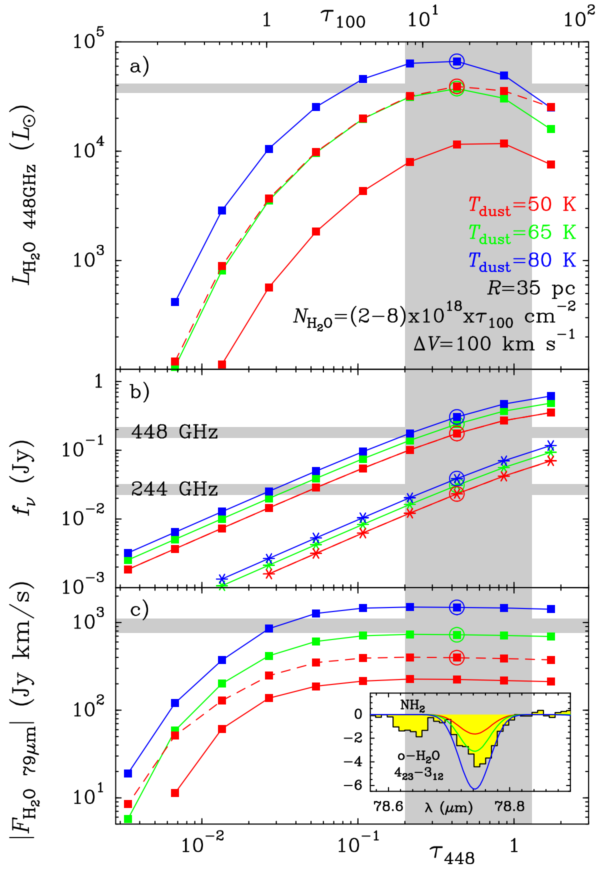

Fig. 5. a) Model predictions showing the luminosity of the H_2O 448 GHz line as a function of the continuum optical depth at 448 GHz (τ_{448}, lower axis) and at 100 μm (τ_{100}, upper axis), for uniform $T_{\rm dust}$ = 50, 65, and 80 K. The models assume spherical symmetry with a radius R = 35 pc. The assumed H_2O abundance is $X(H_2O) = 1.5 \times 10^{-6}$ (solid lines) and $X(H_2O) = 6 \times 10^{-6}$ (dashed red line). The shadowed regions mark the favored ranges inferred from the ESO 320-G030 observations. **b)** Comparison between the predicted continua at 448 GHz (squares) and 244 GHz (starred symbols) and the observed values (after subtracting the free-free emission; horizontal stripes). **c)** Comparison between the predicted absorbing flux of the pumping H_2O 4_{23}–3_{12} line at 79 μm and the observed value (-920 Jy km s^{-1} within ±150 km s^{-1}; horizontal stripe). The insert compares the observed H_2O 4_{23}–3_{12} absorption at 78.7 μm with the predictions of the three models encircled in the three panels. The widths of the horizontal stripes assume uncertainties of $\pm10\%$ for $L_{H_2O\,448}$, and $\pm20\%$ for the continuum flux densities and for the flux of the H_2O 79 μm line.

We also determined the spatially resolved kinematics of the water emission by fitting a Gaussian profile pixel by pixel. The velocity field of the water line is shown in Fig. 4 for the pixels where the line is detected at $>3\sigma$. It shows a clear rotating pattern whose kinematic axes are approximately aligned with the large-scale kinematic axes derived from both the CO(2–1) and Hα emissions (PS16; Bellocchi et al. 2013). The slight angular deviation, ~25°, is similar to that observed in the nuclear CO(2–1) kinematics and might be related to the secondary stellar bar and the elongated molecular structure associated with this bar (PS16). The FWHM line width ranges from ~100–170 km s^{-1} with the maximum value close to the water emission peak.

Based on the measured continuum fluxes at 448 GHz and 244 GHz (PS16), and on the emitting region size, we estimated the dust temperature and optical depth. First, we subtracted the free-free contribution at these frequencies (~7 mJy; PS16). Then, we solved the gray-body equation assuming $1.5 < \beta < 1.85$ and using a Monte Carlo bootstrapping method to estimate the confidence intervals. We find that $T_{\rm dust}$ = 25–80 K and $\tau_{448\,\rm GHz}$ = 0.2–1.3. These values may be significantly higher in the more compact region sampled by the H_2O 448 GHz emission.

4. Modeling the H_2O 448 GHz emission

Figure 5a shows the model predictions for the H_2O 448 GHz luminosity as a function of the continuum optical depth for different dust temperatures ($T_{\rm dust}$ = 50, 65, and 80 K). The models, based on those reported in GA14, use the observed size (R = 35 pc) and assume a H_2O column density of N_{H_2O} = $2 \times 10^{18} \times \tau_{100}$ (solid lines) and $8 \times 10^{18} \times \tau_{100}$ (dashed red line). These values correspond to H_2O abundances relative to H nuclei of $X_{H_2O} = 1.5 \times 10^{-6}$ and 6×10^{-6}, respectively, for a standard gas-to-dust ratio of 100 by mass. The horizontal shaded rectangle indicates the measured value of $3.8 \times 10^4\ L_\odot$, and the vertical shaded rectangle highlights the observationally favored $\tau_{448} \gtrsim 0.2$, corresponding to $\tau_{100} \gtrsim 8$.

At low column densities, $L_{\mathrm{H_2O\,448}}$ increases sharply with τ_{448} due to the enhancement of the far-IR radiation field, responsible for the H_2O excitation, and to the increase of $N_{\mathrm{H_2O}}$. The H_2O 448 GHz line is not masing, but usually shows suprathermal excitation ($T_{\mathrm{EX}} > T_{\mathrm{dust}}$) in some shells.

The excitation is dominated in all cases by radiative pumping through the $4_{23}-3_{12}$ and $4_{23}-4_{14}$ lines at 78.7 and 132.4 μm (Fig. 1). Collisional excitation (included in the models with $n_{\mathrm{H2}} = 3 \times 10^4\ \mathrm{cm^{-3}}$ and $T_{\mathrm{gas}} = 150$ K) has the effect of increasing the population of the low-lying levels from which the radiative pumping cycle works (see GA14) thus still having an overall effect on line fluxes. As τ_{100} increases above unity, the increase in τ_{100} only slightly enhances the far-IR radiation field and $L_{\mathrm{H_2O\,448}}$ flattens. It is only in this regime that $L_{\mathrm{H_2O\,448}}$ approaches the observed value for high enough $T_{\mathrm{dust}} \gtrsim 65$ K or $N_{\mathrm{H_2O}} = 8 \times 10^{18} \times \tau_{100}$, indicating that the H_2O 448 GHz line is an excellent probe of buried galaxy nuclei. At higher τ_{100}, line opacity effects and extinction effects at 448 GHz (for τ_{448} approaching unity) decrease $L_{\mathrm{H_2O\,448}}$.

With an adopted H_2O abundance of 1.5×10^{-6} and $T_{\mathrm{dust}} \sim 65$ K (green lines and symbols), we can approximately match the observed H_2O 448 GHz emission (Fig. 5a), and the 448 and 244 GHz continuum emissions (Fig. 5b) for $\tau_{448} \approx 0.3$. However, the same observables can also be fitted, for $\tau_{448} = 0.4-0.6$, with a higher $X_{\mathrm{H_2O}} = 6 \times 10^{-6}$ and a more moderate $T_{\mathrm{dust}} = 50$ K (red-dashed lines). We can discriminate between both solutions by noting that the dust opacity conditions required for the H_2O 448 GHz line to emit efficiently, $\tau_{100} > 1$, are similar to the conditions required to have strong absorption in the high-lying H_2O lines at far-IR wavelengths (e.g., González-Alfonso et al. 2012; Falstad et al. 2017), strongly suggesting that both the 448 GHz emission line and the far-IR absorption lines arise in similar regions. One of the main H_2O lines responsible for the pumping of the H_2O 448 GHz transition, the $4_{23}-3_{12}$ line at $\approx$79 μm (Fig. 1), was observed with *Herschel*/PACS (Pilbratt et al. 2010; Poglitsch et al. 2010) within the open time program HerMoLIRG (PI: E. González-Alfonso; OBSID = 1342248549). We compare in Fig. 5c the predicted absorbing flux in this line and the observed value (-920 Jy km s^{-1} between -150 and $+150$ km s^{-1}, the observed velocity range of the H_2O 448 GHz line at zero intensity; see Fig. 3). While the $T_{\mathrm{dust}} \sim 50$ K model underpredicts the pumping H_2O 79 μm absorption, the $T_{\mathrm{dust}} \sim 65$ K model better accounts for it, with still some unmatched redshifted absorption (see insert in Fig. 5c). We thus conclude that the H_2O 448 GHz line originates in warm regions ($T_{\mathrm{dust}} \gtrsim 60$ K).

Our favored models indicate that the luminosity of the nuclear region where the H_2O 448 GHz arises is $(4-6) \times 10^{10}\ L_\odot$, that is, $\sim$25% of the total galaxy luminosity. While approximately accounting for the observables reported in this *Letter* ($L_{\mathrm{H_2O\,448}}$, allowed τ_{448} range, f_{448}, f_{244}, and $4_{23}-3_{12}$ absorption strength for the observed size), we advance the *Herschel* detection of very-high-lying H_2O absorption lines indicating the presence of an additional warmer component in the nuclear region of ESO 320-G030. The full set of H_2O (and OH) lines will be studied in a future work.

5. Conclusions

We detected the ortho-H_2O $4_{23}-3_{30}$ transition at 448 GHz using ALMA observations of the local spiral LIRG ESO 320-G030. The H_2O 448 GHz emission arises from the highly obscured nucleus of this galaxy and is spatially resolved ($r \sim 30$ pc). The H_2O 448 GHz velocity field is compatible with the global regular rotation pattern of the molecular and ionized gas in ESO 320-G030. Our radiative transfer modeling shows that it is mainly excited by the intense far-IR radiation field present in the nucleus of this source. The conditions for the excitation of the 448 GHz water transition indicate that it can probe deeply buried, warm environments both locally and at high redshifts.

Acknowledgements. We thank the anonymous referee for useful comments and suggestions. We thank M. Villar-Martín and S. Motta for useful comments and careful reading of the manuscript. M.P.S. acknowledges support from STFC through grant ST/N000919/1, the John Fell Oxford University Press (OUP) Research Fund and the University of Oxford. E.G.S., A.U., S.G.B., J.M.P., L.C., A.A.H., S.A., S.C., and F.R.V. acknowledge financial support by the Spanish MEC under grants ESP2015-65597-C4-1-R, AYA2012-32295, ESP2015-68694, AYA2013-42227-P and AYA2015-64346-C2-1-P, which is partly funded by the FEDER programme. E.G.A. a Research Associate at the Harvard-Smithsonian CfA and acknowledges support by NASA grant ADAP NNX15AE56G. This paper makes use of the following ALMA data: ADS/JAO.ALMA#2016.1.00263.S. ALMA is a partnership of ESO (representing its member states), NSF (USA) and NINS (Japan), together with NRC (Canada) and NSC and ASIAA (Taiwan) and KASI (Republic of Korea), in cooperation with the Republic of Chile. The Joint ALMA Observatory is operated by ESO, AUI/NRAO and NAOJ.

References

Arribas, S., Colina, L., Bellocchi, E., Maiolino, R., & Villar-Martín, M. 2014, A&A, 568, A14
Bellocchi, E., Arribas, S., Colina, L., & Miralles-Caballero, D. 2013, A&A, 557, A59
Bellocchi, E., Arribas, S., & Colina, L. 2016, A&A, 591, A85
Briggs, D. S. 1995, Ph.D. Thesis, New Mexico Institute of Mining and Technology
Cazzoli, S., Arribas, S., Colina, L., et al. 2014, A&A, 569, A14
Cazzoli, S., Arribas, S., Maiolino, R., & Colina, L. 2016, A&A, 590, A125
Cooke, B., & Elitzur, M. 1985, ApJ, 295, 175
Daniel, F., & Cernicharo, J. 2013, A&A, 553, A70
Deguchi, S. 1977, PASJ, 29, 669
Falstad, N., González-Alfonso, E., Aalto, S., & Fischer, J. 2017, A&A, 597, A105
Flower, D. R., & Pineau Des Forêts, G. 2010, MNRAS, 406, 1745
González-Alfonso, E., Fischer, J., Graciá-Carpio, J., et al. 2012, A&A, 541, A4
González-Alfonso, E., Fischer, J., Aalto, S., & Falstad, N. 2014, A&A, 567, A91
González-Alfonso, E., Fischer, J., Spoon, H. W. W., et al. 2017, ApJ, 836, 11
Gray, M. D., Baudry, A., Richards, A. M. S., et al. 2016, MNRAS, 456, 374
Hollenbach, D., Kaufman, M. J., Bergin, E. A., & Melnick, G. J. 2009, ApJ, 690, 1497
Lo, K. Y. 2005, ARA&A, 43, 625
McMullin, J. P., Waters, B., Schiebel, D., Young, W., & Golap, K. 2007, in Astronomical Data Analysis Software and Systems XVI, eds. R. A. Shaw, F. Hill, & D. J. Bell, ASP Conf. Ser., 376, 127
Neufeld, D. A., & Melnick, G. J. 1991, ApJ, 368, 215
Norris, R. P., Whiteoak, J. B., Gardner, F. F., Allen, D. A., & Roche, P. F. 1986, MNRAS, 221, 51P
Pereira-Santaella, M., Alonso-Herrero, A., Rieke, G. H., et al. 2010, ApJS, 188, 447
Pereira-Santaella, M., Alonso-Herrero, A., Santos-Lleo, M., et al. 2011, A&A, 535, A93
Pereira-Santaella, M., Colina, L., García-Burillo, S., et al. 2016, A&A, 594, A81
Persson, C. M., Olofsson, A. O. H., Koning, N., et al. 2007, A&A, 476, 807
Pickett, H. M., Poynter, R. L., Cohen, E. A., et al. 1998, J. Quant. Spectr. Rad. Transf., 60, 883
Pilbratt, G. L., Riedinger, J. R., Passvogel, T., et al. 2010, A&A, 518, L1
Poglitsch, A., Waelkens, C., Geis, N., et al. 2010, A&A, 518, L2
Sakamoto, K., Wang, J., Wiedner, M. C., et al. 2008, ApJ, 684, 957
van Dishoeck, E. F., Herbst, E., & Neufeld, D. A. 2013, Chem. Rev., 113, 9043
Wiggins, B. K., Migenes, V., & Smidt, J. M. 2016, ApJ, 816, 55
Yates, J. A., Field, D., & Gray, M. D. 1997, MNRAS, 285, 303